ADVANCED ENERGY MATERIALS
www.advenergymat.de

Mixed Cation $FA_xPEA_{1-x}PbI_3$ with Enhanced Phase and Ambient Stability toward High-Performance Perovskite Solar Cells

Nan Li, Zonglong Zhu, Chu-Chen Chueh, Hongbin Liu, Bo Peng, Alessio Petrone, Xiaosong Li, Liduo Wang, and Alex K.-Y. Jen**

In this work, different from the commonly explored strategy of incorporating a smaller cation, MA^+ and Cs^+ into $FAPbI_3$ lattice to improve efficiency and stability, it is revealed that the introduction of phenylethylammonium iodide (PEAI) into $FAPbI_3$ perovksite to form mixed cation $FA_xPEA_{1-x}PbI_3$ can effectively enhance both phase and ambient stability of $FAPbI_3$ as well as the resulting performance of the derived devices. From our experimental and theoretical calculation results, it is proposed that the larger PEA cation is capable of assembling on both the lattice surface and grain boundaries to form quais-3D perovskite structures. The surrounding of PEA^+ ions at the crystal grain boundaries not only can serve as molecular locks to tighten $FAPbI_3$ domains but also passivate the surface defects to improve both phase and moisture stablity. Consequently, a high-performance (PCE:17.7%) and ambient stable $FAPbI_3$ solar cell could be developed.

1. Introduction

Recently, organic–inorganic metal halide perovskites have drawn tremendous research attention among the photovoltaic (PV) community due to their superior semiconducting properties and facile solution processability.[1] To date, the dynamic research efforts have resulted in very high power conversion efficiency (PCE) in derived perovskite solar cells (PVSCs) with the highest certified PCE reaching 22.1%,[2] which is on par with other high-performance inorganic solar cells.[3]

3D hybrid organic–inorganic perovskites are materials with a ABX_3 crystal structure, where A^+ is an organic cation or cesium cation (Cs^+), B^+ is a metal cation, and X^- is a halide anion, respectively.[4] In principle, the electronic band structures of a hybrid perovskite are governed by the electronic orbitals of B^+ and X^- ions, while A^+ ions are mainly responsible for keeping the electroneutrality and cohesion of the lattices.[5] Therefore, the A^+ plays a critical role in affecting the symmetry of perovskite lattice and the associated phase transformation, which will also influence the resulting band structures and relevant optoelectronic properties.[6] In general, if the size of A^+ is too large, the 3D framework of ABX_3 will be transformed into a lower dimensional crystal structure, such as a 2D layered structure.[7]

Currently, methylammonium lead iodide ($MAPbI_3$) is the most commonly studied perovskite composition for high-performance PVSCs.[8] However, there are several issues that need to be addressed, such as the photo- and thermal-stability of $MAPbI_3$.[3,9] This is attributed to its low crystallization energy and low temperature phase transformation between the tetragonal and cubic phase at ≈320 K.[10] Hence, a significant part of research focus has been shifted to engineer the perovskite compositions for achieving optimal material systems.[11]

In this regard, formamidinium lead iodide ($FAPbI_3$) has been vigorously investigated due to its broader light absorption that extends to near infrared (NIR) region, higher decomposition temperature (over 150 °C), and decent charge diffusion length compared to $MAPbI_3$.[12] However, the phase-purity and phase-stability of pristine $FAPbI_3$ have also been found as a significant hurdle for developing efficient and stable PVSC. The relatively easy conversion of black α-phase $FAPbI_3$ into yellow non-perovskite δ-phase limits the resultant photovoltaic performance and long-term stability of devices.[13] These deficiencies need careful investigation to improve their applicability for practical solar cells.[14]

Several research groups have recently unveiled that phase instability of $FAPbI_3$ can be effectively modulated by employing the mixed-cation strategy to form perovskites. For example, by mixing FA^+ with a smaller cation like MA^+ or Cs^+ into $FAPbI_3$, the lattice contraction introduced by the added small cations not only can facilitate the formation of α-phase but also retard its relaxation back to δ-phase.[15] As a result, the current

N. Li, Dr. Z. Zhu, Dr. C.-C. Chueh, Prof. A. K.-Y. Jen
Department of Materials Science & Engineering
University of Washington
Seattle, WA 98195, USA
N. Li, Prof. L. Wang
Key Lab of Organic Optoelectronics & Molecular Engineering of Ministry of Education
Department of Chemistry
Tsinghua University
Beijing 100084, China
E-mail: chldwang@mail.tsinghua.edu.cn
H. Liu, Dr. B. Peng, Dr. A. Petrone, Prof. X. Li, Prof. A. K.-Y. Jen
Department of Chemistry
University of Washington
Seattle, WA 98195, USA
E-mail: ajen@u.washington.edu

DOI: 10.1002/aenm.201601307

 © 2016 WILEY-VCH Verlag GmbH & Co. KGaA, Weinheim

state-of-the-art mix-cation MA^+/FA^+ based PVSC showed a very high PCE of ≈21%.[16] Despite the vigorous progress, the FA-based perovskites still suffer from unsatisfied moisture stability as a result of their easy hydration with H_2O.[17] Therefore, it is imperative to simultaneously improve both their phase and ambient stability.[18]

As mentioned earlier, a 2D layered perovskite will form if the size of the employed A^+ exceeds the tolerance space of a 3D perovskite framework. For example, the phenylethylammonium iodide (PEAI) has been used to form 2D PEA_2PbI_4 perovskite, wherein a bilayered PEA^+ self-assembles along the inorganic sheet consisting of metal halide octahedron.[19] This 2D structure yields a better ambient stability than that of the 3D counterpart due to the stronger interlock between the organic and inorganic species.[20] Based on this principle, several reports have recently described the intercalation of PEA^+ into $MAPbI_3$ to form 2D/3D (or quasi-3D) hybrid perovskites with improved ambient stability.[7a,21] The inserted PEA^+ can break the 3D perovskite framework to result in quasi-3D perovskite structures with hydrophobic PEA formed on the surface to improve the ambient stability of resultant perovskites.

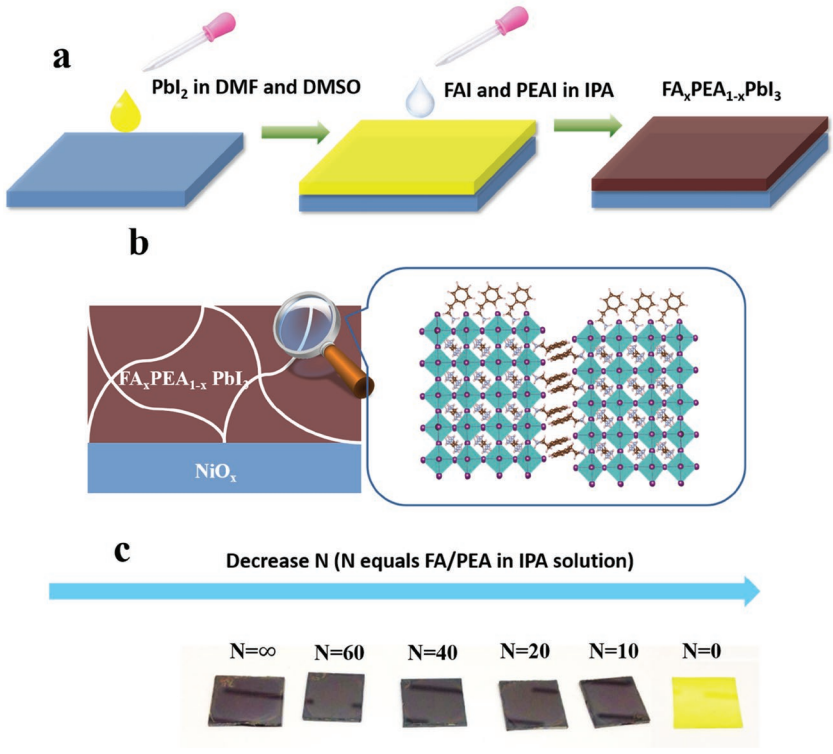

Figure 1. Schematic drawing of a) the deposition of $FA_xPEA_{1-x}PbI_3$ films in this study. b) The formation of quasi-3D $FA_xPEA_{1-x}PbI_3$ crystal. c) Photographs of the prepared $FA_xPEA_{1-x}PbI_3$ films, where N is the molar ratio of FA^+ to PEA^+.

In this work, different from the explored strategy of incorporating a smaller cation, MA^+ or Cs^+, into $FAPbI_3$ lattice, the larger PEA^+ was incorporated into $FAPbI_3$ perovskite to form $FA_xPEA_{1-x}PbI_3$ to demonstrate enhanced phase and ambient stability in addition to obtaining higher photovoltaic performance in derived PVSC. From both experimental results and theoretical calculations, the $FA_xPEA_{1-x}PbI_3$ phase stability was shown to greatly improve in quasi-3D perovskite at room temperature. We hypothesize that PEA^+ might migrate into the $FAPbI_3$ grain boundaries to form a self-assembled organic shell with induced π–π interactions, raising the phase transition energy and enhance its phase stability. In addition, the hydrophobicity of self-assembled PEA^+ layer helps prevent moisture from interacting with $FA_xPEA_{1-x}PbI_3$. The PEA^+ and its I^- counterion can also passivate the surface defects of perovskites to enhance device performance. As a result, a high-performance (PCE: 17.7%) solar cell with superior phase and ambient stability was successfully demonstrated.

2. Results and Discussion

A sequential two-step deposition procedure is employed to process the $FA_xPEA_{1-x}PbI_3$ films in this study (**Figure 1**a), where a PbI_2 layer is formed initially then the FAI or FAI/PEAI mixed solution is deposited on top of layered PbI_2 to convert it into perovskites. The detailed process information is described in the Experiment Section. By adopting this two-step procedure, we speculate that the interdiffusion of FAI/PEAI into the pre-deposited PbI_2 matrix can modulate the PEA^+ distribution and self-assembly on both the top surface and grain boundaries of $FAPbI_3$ as considering their distinct diffusivity and van de Waals interactions between FA^+ and PEA^+.[21b,22]

Previous reports have shown that the incorporation of larger organic cations can result in mixed 2D/3D perovskites with their crystal growth direction perpendicularly oriented to the substrate.[21b,22a] Figure 1b illustrates the schematic drawing of self-assembled PEA^+ in perovskite films. The PEA layer is proposed to form both on the lattice surface and within the grain boundaries via self-assembly to form quasi-3D perovskite structures. Different molar ratios (N) of FAI to PEAI could be adjusted by adding PEAI into the FAI solution. A yellow 2D PEA_2PbI_4 film will form if only a pure PEAI precursor solution is added (Figure 1c). Figure S1 of the Supporting Information presents the top-sectional scanning electron microscopy (SEM) images of the prepared $FA_xPEA_{1-x}PbI_3$ films. All of them exhibit a smooth and homogenous morphology without any pinholes or severe aggregations and possess similar grain sizes. The high quality films are essential for high performance of the derived PVSCs. Shown in Figure S2 of the Supporting Information are the corresponding cross-sectional SEM images of the complete devices, in which similar thickness of the prepared perovskite film can be clearly observed.

The absorption spectra of prepared $FA_xPEA_{1-x}PbI_3$ films are presented in **Figure 2**a. As shown in the spectra, the $FA_xPEA_{1-x}PbI_3$ films possess similar profile with an absorption band-edge around ≈820 nm, and the peak at 500 nm is attributed to the dual valence band structure.[23] To further verify the

© 2016 WILEY-VCH Verlag GmbH & Co. KGaA, Weinheim

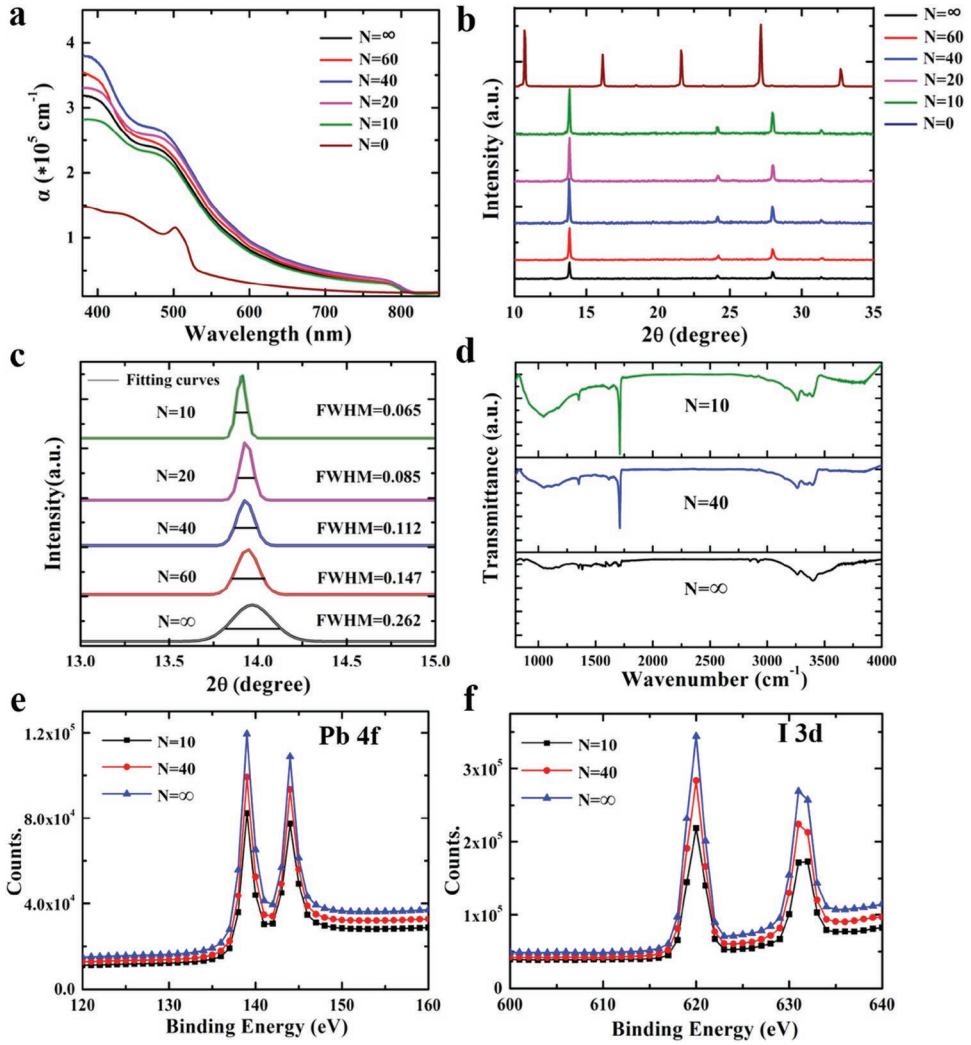

Figure 2. a) Optical absorption spectra, b) XRD patterns, c) magnified (111) peak of XRD patterns, d) FTIR spectra, and e) Pb 4f and f) I 3d XPS spectra of the studied $FA_xPEA_{1-x}PbI_3$ films. N represents the molar ratio of FA^+ to PEA^+.

bandgap of $FA_xPEA_{1-x}PbI_3$ films, we plotted the corresponding transformed Kubelka–Munk (Figure S3, Supporting Information), and the respective bandgap only shows slight increase from 1.518 to 1.524 eV when N increases from 10 to infinity (Table S1, Supporting Information), indicating the main formation of quasi-3D crystalline $FAPbI_3$ domains instead of 2D PEA_2PbI_4 (N = 0) domains. In addition, the total absorbance of $FA_xPEA_{1-x}PbI_3$ films with N between 20 and 60 increases compared to that of the pristine $FAPbI_3$ (N = ∞), suggesting the addition of a small amount of PEA^+ improves the crystallinity of $FAPbI_3$.

The corresponding X-ray diffraction (XRD) patterns are displayed in Figure 2b. For all the quasi-3D $FAPbI_3$ films, the characteristic peaks of ≈13.8°, ≈24.2°, ≈28°, and ≈31.5° can be assigned to the scattering from (111), (021), (222), and (123) crystal planes, which are apparently distinct to the characteristics of 2D PEA_2PbI_4. The full width at half maximum (FWHM) of the peak at ≈13.8° (Figure 2c) was further estimated. The gradually decreased FWHM indicates the decrease of vacancies or dislocation in the perovskite film, given the similar crystal sizes of the prepared $FA_xPEA_{1-x}PbI_3$ films (Figure S1, Supporting Information), which could enhance crystallization of $FAPbI_3$ as a result of PEAI addition. The less vacancies and enhanced crystallization may be due to the self-assembled PEA^+ at the grain boundaries behaving as molecular locks to strengthen the intermolecular interactions of $FAPbI_3$ domains.[7a,21b,24]

To confirm the presence of PEA^+ in the prepared $FA_xPEA_{1-x}PbI_3$ films, we have further applied the Fourier transform infrared spectroscopy (FTIR). In the FTIR spectra (Figure 2d), the feature peak of the alkenyl C=C stretching vibrations from the benzene ring of PEA^+ can be clearly seen at 1600 cm^{-1} and its intensity rises as the amount of incorporated PEA^+ increases. Figure 2e,f shows the X-ray photoelectron spectroscopy (XPS) results of the $FA_xPEA_{1-x}PbI_3$ films processed with N = 10, 40, ∞, respectively. There is no shift of the feature peaks in the XPS spectra of $FA_xPEA_{1-x}PbI_3$ films, suggesting the $FAPbI_3$ chemical bonding among Pb and I atom does not change after incorporating PEA^+, which is in agreement with the UV–vis absorption and XRD results, validating the formation of quasi-3D $FAPbI_3$ as illustrated.

© 2016 WILEY-VCH Verlag GmbH & Co. KGaA, Weinheim

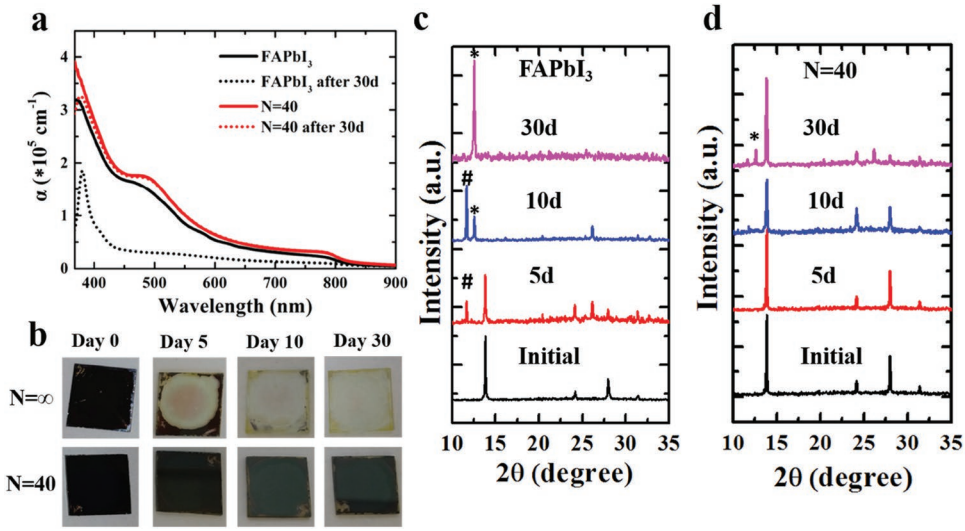

Figure 3. Stability test of pristine $FAPbI_3$ and $FA_xPEA_{1-x}PbI_3$ (N = 40) films: a) UV–vis spectra changes before and after 30 d storage in ambient condition with a relative humidity of 40 ± 5%. b) Photographs of $FA_xPEA_{1-x}PbI_3$ (N = 40) films during the 30 d storage in ambient condition with a relative humidity of 40 ± 5%. XRD pattern spectra of c) pristine $FAPbI_3$ and d) $FA_xPEA_{1-x}PbI_3$ (N = 40) films.

The phase and ambient stability of prepared $FA_xPEA_{1-x}PbI_3$ films are investigated to understand the effect of PEA^+ incorporation on the films stability. All the prepared films were kept in ambient with a relative humidity of around 40 ± 5%. **Figure 3**a shows the corresponding UV–vis spectra recorded at different storage times in ambient. The pristine $FAPbI_3$ decomposes totally into yellow phase after being stored for 30 d while the $FA_xPEA_{1-x}PbI_3$ film (N = 40) shows much better ambient stability. The pictures of degraded films are presented in Figure 3b. The color of pristine $FAPbI_3$ changes from black into yellow after being stored in ambient for 30 d, while the color of the $FA_xPEA_{1-x}PbI_3$ film (N = 40) remains intact in black. Figure 3c,d illustrates the XRD patterns of those degraded films as a function of stored time in ambient, which unravels the possible degradation pathways of these films. The pristine $FAPbI_3$ first converted into δ-phase $FAPbI_3$ (characteristic peak at 11.7°) after 5 d storage in ambient, and then completely degraded into PbI_2 (characteristic peaks at 12.5°) after 30 d. On the contrary, the $FA_xPEA_{1-x}PbI_3$ film (N = 40) shows the retarded yellow phase transformation with only a relatively small amount of perovskite degraded into PbI_2 after 30 d in ambient.

To better understand the reason for the improved phase and ambient stability of $FA_xPEA_{1-x}PbI_3$ film, we resort to the density functional theory (DFT) simulation. On account of the sufficient characterizations, we propose that PEA^+ mainly penetrate into grain boundaries and substitute the FA^+ at the crystal surface. Based on this model, we first studied the stability of α-phase $FAPbI_3$ by calculating the formation energy with different molar fractions of FA^+, and the detailed information is shown in the Supporting Information. By gradually substituting FA^+ with PEA^+ at the crystal surface, the formation energy of α-phase $FAPbI_3$ changes with different molar fractions of FA^+. The system reaches the most stable state of phase with the highest formation energy when the FA^+ molar fraction is around 95% to 96% (Figure S5, Supporting Information).

Based on these calculations, we hypothesize the reason for improved phase stability of $FA_xPEA_{1-x}PbI_3$ film. The α- and δ-phase of $FAPbI_3$ lattices have very similar building layers parallel to the ab plane, which are highlighted with yellow circles in **Figure 4**a,b. The significant difference is that the black phase has one more FAI layer inserted in its supercell structure, which is highlighted in the red circle in Figure 4a. Therefore, it is reasonable to assume that the black phase can turn into the yellow phase through some translations of different layers. In this regard, the existence of PEA^+ interlayer on the (–111) plane surface (Figure 4c) with π–π stacking of benzene ring on the lattice surface and grain boundary might lock the 3D lattice structure, block layer translation pathways, and raise the energy barrier of transition from the black phase to the yellow phase, thus making the black phase PEA-$FAPbI_3$ a kinetically stable substance. Figure 4d gives an illustration of the increased energy barrier of phase transition from theoretical calculation.

The inverted p–i–n planar $FA_xPEA_{1-x}PbI_3$-based PVSCs were fabricated in the configuration of ITO/NiO_x/$FA_xPEA_{1-x}PbI_3$/PCBM/bis-C_{60}/Ag.[11c,25] **Figure 5**a shows a representative cross-sectional SEM image of the fabricated devices, wherein a thick perovskite layer (≈400 nm) was deposited on top of the NiO_x hole-transporting layer (HTL) (≈40 nm), followed by the deposition of a PCBM electron-transporting layer (ETL) (≈50 nm) and a thin bis-C_{60} surfactant layer (≈10 nm). The energy levels of the fabricated device illustrated in Figure 5b show the well aligned conduction band minimum (CBM) and valence band maximum (VBM) of perovskite with the energy levels of employed ETL and HTL, respectively, which ensures the efficient charge transport and collection in the device.

Photocurrent density–voltage (J–V) characteristics (measured under AM1.5G irradiation at 100 mW cm^{-2} with a scan rate of 100 mV s^{-1}) of the studied devices are shown in Figure S6 of the Supporting Information and the detailed photovoltaic parameters are summarized in Tables S2 and S3 of the Supporting Information. The best PCE of 17.71%, with a V_{OC} of

© 2016 WILEY-VCH Verlag GmbH & Co. KGaA, Weinheim

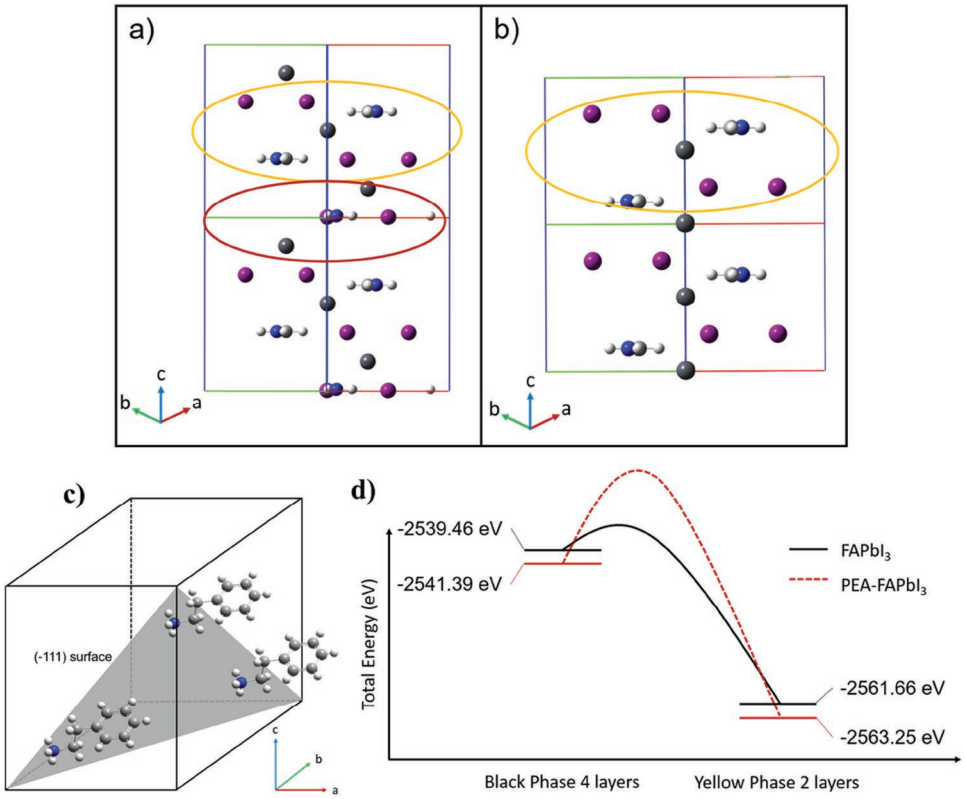

Figure 4. Material calculation: a) The 1 × 1 × 2 supercell of black phase $FAPbI_3$. b) The 1 × 1 × 2 supercell of the yellow phase $FAPbI_3$. c) The PEA docking on the (–111) surface of black phase $FAPbI_3$ will prevent the layer translations or mismatch along the a, b, c directions. d) The thermodynamic analysis and kinetic hypothesis using a four-layer black phase $FAPbI_3$ to a two-layer yellow phase $FAPbI_3$ transition (number of Pb atoms conserved) as an example.

1.04 V, a J_{SC} of 22.08 mA cm^{-2}, and a FF of 77.14% is realized in the device based on a $FA_xPEA_{1-x}PbI_3$ with N = 40 and shows negligible hysteresis under the forward and reverse scans (Figure 5c). The external quantum efficiency (EQE) spectrum is plotted in Figure 5d, for which the integrated J_{SC} agrees well with the value obtained in the *J–V* curve. A plateau of EQE around 80% across 400–750 nm is clearly observed, revealing the high photon-to-electron conversion of the fabricated device. To further confirm the reliability of the fabricated PVSC, the stabilized photocurrent measured at a constant bias of 0.89 V near the maximum power point is examined and presented in Figure 5e. A steady-state PCE of 17.3% is clearly shown. Moreover, the solar cell efficiency histogram of this top-performing PVSC is evaluated along with the Gaussian fitting as illustrated in Figure 5f, which unravels an average PCE of 16.4% over 35 devices with good reproducibility. Figure 5g shows that the ambient stability of the $FA_xPEA_{1-x}PbI_3$ (N = 40) based device is greatly improved, which retains over 90% of its initial PCE after being stored in air for 16 d under a relative humidity of 40 ± 5% without encapsulation. On the contrary, the PCE of pure $FAPbI_3$ based device decays to near zero after 16 d.

It is interesting to note that all the fabricated devices show similar series resistance (R_s) but distinctly different shunt resistance (R_{shunt}), which is relevant to the previously discussed favorable vertical crystal growth induced by the small amount of PEA^+ at the grain boundaries (Figure 1b). The self-assembled PEA^+ layer might induce the vertical growth of crystals upon the substrate to decrease the lateral charge leaking and to increase R_{shunt}, which further reduces the charge recombination of the PVSC devices and thereby leads to increased FF.

Electrochemical impedance spectroscopy (EIS) has been widely used to measure the charge transport dynamics in solar cells, such as chemical capacitance, recombination lifetime, and transport properties.[26] As metioned, the PEA^+ should be located mainly at the perovskite surface and grain boundaries, which will also passivate the grain boundary defects.[21a,24] To further elucidate the charge carrier dynamics in $FA_xPEA_{1-x}PbI_3$, we have measured the EIS for devices derived from $FA_xPEA_{1-x}PbI_3$ (N = 40, 60, and ∞). The Nyquist plots of these devices recorded at different applied voltages are shown in **Figure 6**a–c. The frequency used for all EIS measurements is ranging from 0.5 Hz to 1 MHz. All devices were applied with a bias ranging from 0 to 1 V. The arc at low frequencies has been assigned as the recombination process[27] and the obtained data was fitted based on the commonly used equivalent circuit model as shown in Figure 6d, where a parallel bulk resistance (R_1)–chemical capacitance (C_1) sub-circuit was applied. R_2 represents the surface recombination resistance along with its related capacitance (C_2) forming another sub-circuit, and R_s, C_3, and R_3 represent the series resistance, geometric capacitance, and internal resistance, respectively.[28] The recombination process in device was investigated by evaluating its bulk charge recombination resistance

© 2016 WILEY-VCH Verlag GmbH & Co. KGaA, Weinheim

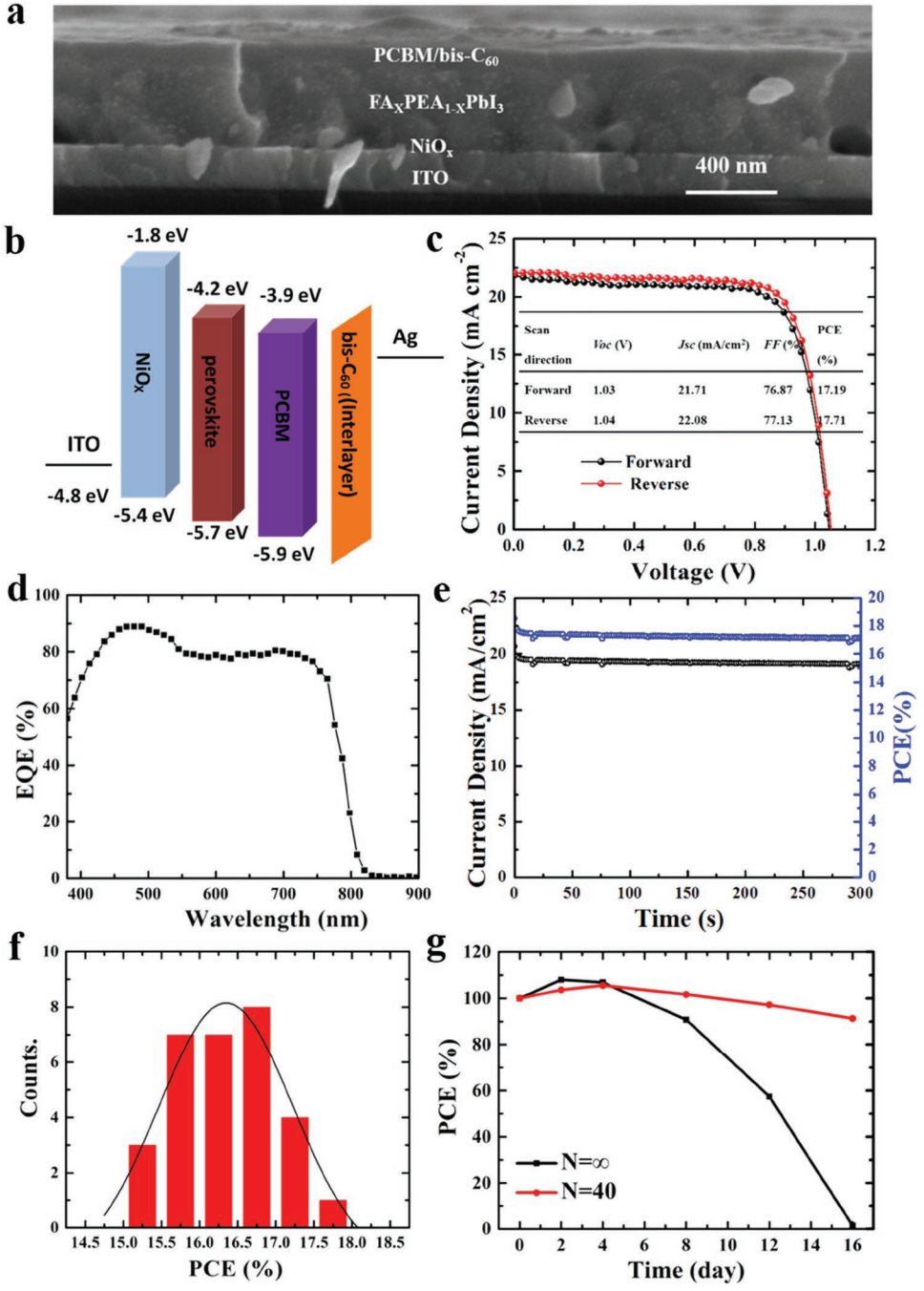

Figure 5. a) The cross-sectional SEM image of the fabricated device. b) The energy level diagram of the studied device with a structure of ITO/NiO_x/$FA_xPEA_{1-x}PbI_3$/PCBM/bis-C_{60}/Ag. c) The *J*–*V* curve, d) EQE spectra, and e) the stable out-put performance curve of $FA_xPEA_{1-x}PbI_3$ devices with the best performance. f) The performance distribution of $FA_xPEA_{1-x}PbI_3$ (N = 40) devices. g) The stability evolution of the derived PVSCs. Note the stabilized photocurrent density (black) and PCE (blue) shown in (e) is measured under a constant bias of 0.89 V near the maximum power point.

(R_{rec}) from R_1, and surface charge recombination resistance ($R_{rec(surface)}$) from R_2, respectively.[27c,28,29] We find that the R_{rec} shares the order of $R_{rec}(N = 10) \approx R_{rec}(N = 40) > R_{rec}(N = \infty)$, and the surface recombination $R_{rec(surface)}$ shares the order of $R_{rec(surface)}$ $(N = 10) > R_{rec(surface)}$ $(N = 40) > R_{rec(surface)}$ $(N = \infty)$ showing a larger difference than R_{rec}. These results suggest that the intercalated PEA^+ can efficiently reduce the surface recombination, demonstrating its possible role in passivating the defects located among the grain boundaries.

3. Conclusions

In summary, we demonstrate that both phase and ambient stability of $FAPbI_3$ can be effectively enhanced by intercalating a

© 2016 WILEY-VCH Verlag GmbH & Co. KGaA, Weinheim

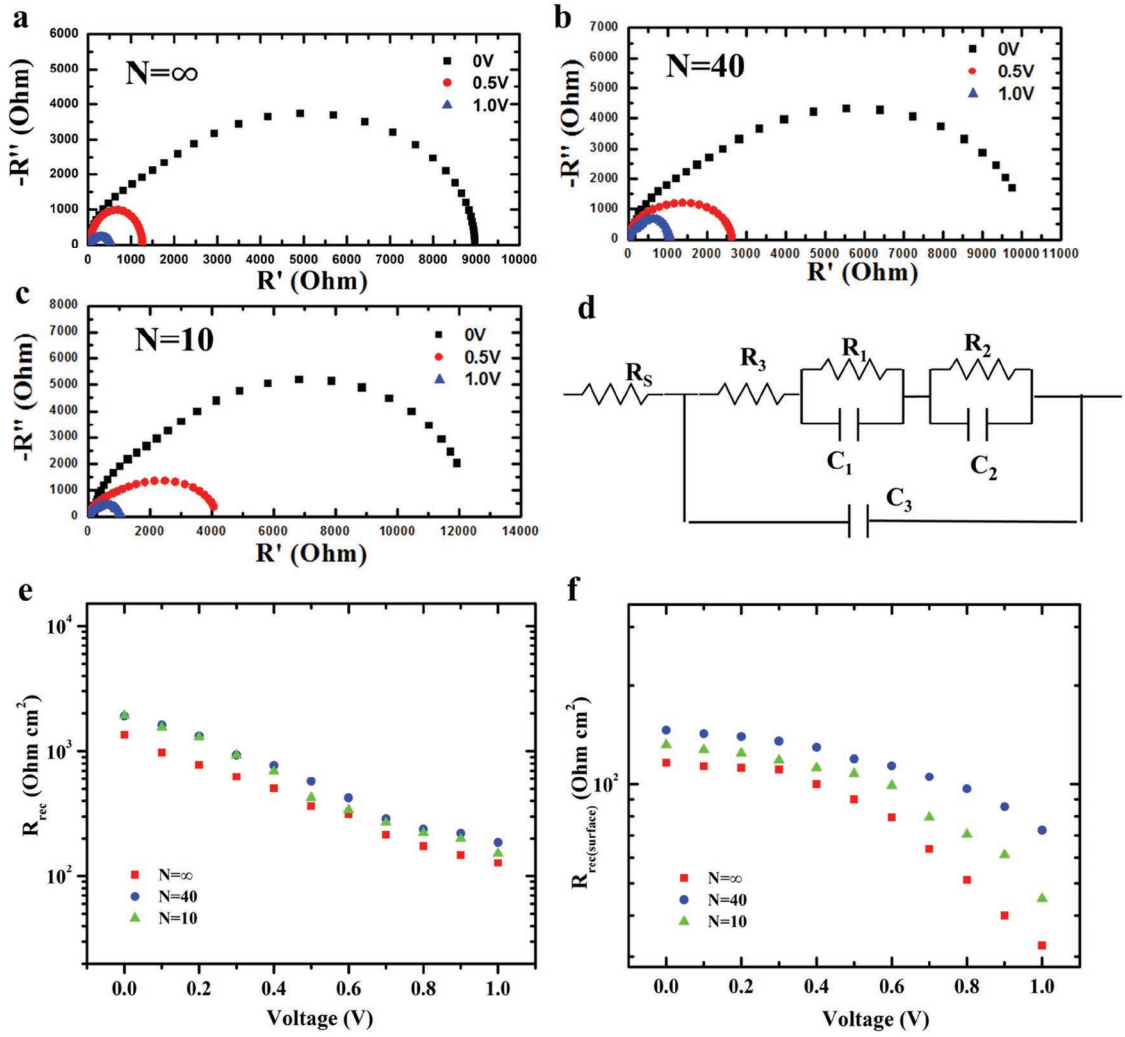

Figure 6. Impedance spectrum study. The representative Nyquist plots of whole regions of impedance spectra at different biases (0, 0.5, and 1.0 V) of a) $FAPbI_3$, $FA_xPEA_{1-x}PbI_3$ (b) N = 40 and c) N = 10) based PVSCs. The equivalent circuit d) is used for fitting the Nyquist plots. Plots a series of e) bulk recombination resistance and f) surface recombination resistance of $FAPbI_3$ and $FA_xPEA_{1-x}PbI_3$ (N = 40 and N = 10) based PVSCs.

larger cation PEA^+ into $FAPbI_3$ perovskite to form mix-cation $FA_xPEA_{1-x}PbI_3$ perovskites. Our theoretical calculation indicates the transition energy from the black phase to the yellow phase is raised to result in enhanced phase stability. Meanwhile, we revealed the PEA^+ and its I^- counterion can also passivate the defects at lattice surface and grain boundaries with the hydrophobic PEA^+, enhancing both the derived device performance and the ambient stability. As a result, a high-performance $FA_xPEA_{1-x}PbI_3$ solar cell with a PCE as high as 17.7% was demonstrated with superior phase and ambient stability. Based on these experimental and theoretical calculation results, we propose that PEA^+ can self-assemble at the lattice surface and grain boundaries of 3D perovskite grains to form quasi-3D perovskite structures via a two-step deposition, behaving as molecular locks to strengthen the intermolecular interactions of $FAPbI_3$. The detailed mode and position of the incorporated PEA^+ in $FAPbI_3$ warrants more specific analysis and in situ characterization and more in-depth investigation is in progress.

4. Experimental Section

Materials: Lead iodide, nickel acetate tetrahydrate, and [6,6]-phenyl-C61-butyric acid methylester ($PC_{61}BM$) were purchased from Sigma-Aldrich. Formamidinium iodide and phenylethylammonium iodide was synthesized according to previously reported methods.[12a,21a] Bis-C_{60} was synthesized as reported in our previous work.[25a]

Solution Preparation: A nickel oxide precursor solution was prepared as reported in the previous work.[11c] PbI_2 solution was prepared in mixed dimethyl formamide (DMF) and dimethyl sulfoxide (DMSO) solvent with a concentration of 1 mmol mL^{-1}. 30 mg FAI was dissolved in 1 mL isopropanol (IPA). PEAI with different molar ratio fractions to FAI was added in FAI solution. 15 mg $PC_{61}BM$ was dissolved into 1 mL chloroform. Bis-C_{60} solution was prepared by dissolving 2 mg bis-C_{60} into 1 mL IPA, followed by sonication for 1 h.

Perovskite Solar Cell Fabrication and Characterization: ITO glass (15 Ω sq^{-1}) was cleaned by sequential sonication with a detergent solution, deionized water, acetone, and isopropyl alcohol for 10 min, respectively. After dried by a nitrogen flow, the substrates were further treated with UV ozone for 10 min before use. NiO_x films were fabricated by spin coating the precursor solution onto the ITO substrates

© 2016 WILEY-VCH Verlag GmbH & Co. KGaA, Weinheim

at 3000 rpm for 60 s, followed by annealing at 400 °C for 1 h in air. After cooled down to the room temperature, NiO_x films were transferred into the N_2 glovebox. To fabricate perovskite films, first PbI_2 solution was spin coated at 4000 rpm for 30 s followed by annealing at 70 °C for 10 min. Sequentially, the FAI solution or the mixed PEAI and FAI solution was loaded on the PbI_2 film for 15 s before spin coated at 4000 rpm for 20 s and annealed at 150 °C for 15 min. Then the $PC_{61}BM$ solution and bis-C_{60} surfactant solution were spin coated at 4000 rpm for 60 s and 3000 rpm for 60 s sequentially. Finally, 150 nm silver was evaporated as the electrode through a 3.14 mm^2 thin mask under high vacuum ($<1 \times 10^{-6}$ Torr). For all studied devices, the device area was defined as 3.14 mm^2 by metal shadow mask.

The morphology and structure of the perovskite films were characterized by SEM (FEI Sirion XL30 SEM operated at 5 kV) and XRD (Bruker F8 Focus Powder XRD), respectively. The absorption spectra were measured by a Varian Cary 5000 UV–vis-NIR. FT-IR spectra were collected by Bruker Vector 33 Fourier transform infrared spectrophotometer. XPS was collected from a SSI S-Probe XPS system Surface Science Instruments, Mountain View, CA using a monochromatic Al $\alpha_{1,2}$ X-ray source $h\nu$ = 1486.6 eV. The *J*–*V* curves and steady-state power output of the perovskite solar cells were measured by a Keithley 2400 Source Meter under illumination by a 450 W Oriel xenon lamp with an AM1.5G filter solar simulator (100 mW cm^{-2}), and the light intensity was calibrated with a standard Si photodiode detector (equipped with a KG-5 filter). The EQE spectra were measured using a setup consisting of a xenon lamp (Oriel, 300 W) as a light source, a monochromator (Newport Cornerstone 130), a chopper with a frequency of 100 Hz, a lock-in amplifier (Stanford Research Corp SR830), a SMU (Keithley 2400), and a NIST-certified Si-photodiode (Thorlabs FDS 100-CAL) for calibration. White light bias was applied using a 50 W LED fiber optic illuminator; no change was observed in the EQE measurements with and without white light bias. The EQE spectrum w as integrated over AM1.5G photon-flux to attain photocurrent density. The fluctuation of xenon arc lamp source was within 5% during the entire period of measurement. We measured the EIS spectra at an applied bias and a frequency ranging between 1 Hz and 1 MHz with AC amplitude of 10 mA. The Z-View Analyst software was used to model the Nyquist plots obtained from the impedance measurements.

Supporting Information

Supporting Information is available from the Wiley Online Library or from the author.

Acknowledgements

This work was supported by the Office of Naval Research (N00014-14-1-0246), the Asian Office of Aerospace R&D (FA2386-15-1-4106), the Department of Energy SunShot (DE-EE0006710) and the National Natural Science Foundation of China under Grant No. 51273104 and 91433205. A.K.-Y.J. thanks the Boeing-Johnson Foundation for financial support. Computations were conducted through the use of advanced computational, storage, and networking infrastructure provided by the Hyak supercomputer system at the University of Washington, funded by the Student Technology Fee. N.L. thanks China Scholarship Council (201506210171) for financial support. Theoretical research is supported by the National Science Foundation (CHE-1464497 and CHE-1565520 to X.L.).

Received: June 16, 2016
Revised: August 10, 2016
Published online:

[1] a) C.-C. Chueh, C.-Z. Li, A. K.-Y. Jen, *Energy Environ. Sci.* **2015**, *8*, 1160; b) W.-J. Yin, J.-H. Yang, J. Kang, Y. Yan, S.-H. Wei, *J Mater. Chem. A* **2015**, *3*, 8926; c) S. D. Stranks, H. J. Snaith, *Nat. Nanotechnol.* **2015**, *10*, 391; d) M. A. Green, A. Ho-Baillie, H. J. Snaith, *Nat. Photonics* **2014**, *8*, 506.

[2] NREL efficiency chart, http://www.nrel.gov/ncpv/images/efficiency_chart.jpg (accessed: June, 2016).

[3] S. T. Williams, A. Rajagopal, C.-C. Chueh, A. K.-Y. Jen, *J Phys. Chem. Lett.* **2016**, *7*, 811.

[4] a) P. Gao, M. Gratzel, M. K. Nazeeruddin, *Energy Environ. Sci.* **2014**, *7*, 2448; b) H. S. Jung, N.-G. Park, *Small* **2015**, *11*, 10; c) H.-S. Kim, S. H. Im, N.-G. Park, *J. Phys. Chem. C* **2014**, *118*, 5615; d) N.-G. Park, *J. Phys. Chem. Lett.* **2013**, *4*, 2423; e) H. J. Snaith, *J. Phys. Chem. Lett.* **2013**, *4*, 3623; f) T. C. Sum, N. Mathews, *Energy Environ. Sci.* **2014**, *7*, 2518.

[5] a) W.-J. Yin, T. Shi, Y. Yan, *Adv. Mater.* **2014**, *26*, 4653; b) W.-J. Yin, T. Shi, Y. Yan, *Appl. Phys. Lett.* **2014**, *104*, 063903/1.

[6] a) Q. Lin, A. Armin, P. L. Burn, P. Meredith, *Acc. Chem. Res.* **2016**, *49*, 545; b) J. S. Manser, M. I. Saidaminov, J. A. Christians, O. M. Bakr, P. V. Kamat, *Acc. Chem. Res.* **2016**, *49*, 330; c) Y. Yuan, J. Huang, *Acc. Chem. Res.* **2016**, *49*, 286; d) A. R. b. M. Yusoff, M. K. Nazeeruddin, *J. Phys. Chem. Lett.* **2016**, *7*, 851; e) S. T. Williams, C.-C. Chueh, A. K.-Y. Jen, *Small* **2015**, *11*, 3088.

[7] a) I. C. Smith, E. T. Hoke, D. Solis-Ibarra, M. D. McGehee, H. I. Karunadasa, *Angew. Chem.* **2014**, *126*, 11414; b) Z. Cheng, J. Lin, *CrystEngComm* **2010**, *12*, 2646; c) P. P. Boix, S. Agarwala, T. M. Koh, N. Mathews, S. G. Mhaisalkar, *J. Phys. Chem. Lett.* **2015**, *6*, 898.

[8] a) J. Seo, J. H. Noh, S. I. Seok, *Acc. Chem. Res.* **2016**, *49*, 562; b) J. Burschka, N. Pellet, S.-J. Moon, R. Humphry-Baker, P. Gao, M. K. Nazeeruddin, M. Graetzel, *Nature* **2013**, *499*, 316; c) M. M. Lee, J. Teuscher, T. Miyasaka, T. N. Murakami, H. J. Snaith, *Science* **2012**, *338*, 643; d) A. Rajagopal, S. T. Williams, C.-C. Chueh, A. K.-Y. Jen, *J. Phys. Chem. Lett.* **2016**, *7*, 995; e) W. Nie, H. Tsai, R. Asadpour, J.-C. Blancon, A. J. Neukirch, G. Gupta, J. J. Crochet, M. Chhowalla, S. Tretiak, M. A. Alam, H.-L. Wang, A. D. Mohite, *Science* **2015**, *347*, 522.

[9] H. Yu, F. Wang, F. Xie, W. Li, J. Chen, N. Zhao, *Adv. Funct. Mater.* **2014**, *24*, 7102.

[10] a) Q. Lin, A. Armin, P. L. Burn, P. Meredith, *Acc. Chem. Res.* **2016**, *49*, 545; b) A. R. Srimath Kandada, A. Petrozza, *Acc. Chem. Res.* **2016**, *49*, 536; c) B. Wu, H. T. Nguyen, Z. Ku, G. Han, D. Giovanni, N. Mathews, H. J. Fan, T. C. Sum, *Adv. Energy Mater.* **2016**, *6*, 201600551.

[11] a) Q. Chen, H. Zhou, T.-B. Song, S. Luo, Z. Hong, H.-S. Duan, L. Dou, Y. Liu, Y. Yang, *Nano Lett.* **2014**, *14*, 4158; b) N. J. Jeon, J. H. Noh, W. S. Yang, Y. C. Kim, S. Ryu, J. Seo, S. I. Seok, *Nature* **2015**, *517*, 476; c) Z. Yang, C.-C. Chueh, P.-W. Liang, M. Crump, F. Lin, Z. Zhu, A. K.-Y. Jen, *Nano Energy* **2016**, *22*, 328.

[12] a) G. E. Eperon, S. D. Stranks, C. Menelaou, M. B. Johnston, L. M. Herz, H. J. Snaith, *Energy Environ. Sci.* **2014**, *7*, 982; b) N. Pellet, P. Gao, G. Gregori, T.-Y. Yang, M. K. Nazeeruddin, J. Maier, M. Graetzel, *Angew. Chem. Int. Ed.* **2014**, *53*, 3151; c) J.-W. Lee, D.-J. Seol, A.-N. Cho, N.-G. Park, *Adv. Mater.* **2014**, *26*, 4991; d) A. Amat, E. Mosconi, E. Ronca, C. Quarti, P. Umari, M. K. Nazeeruddin, M. Grätzel, F. De Angelis, *Nano Lett.* **2014**, *14*, 3608; e) F. Wang, H. Yu, H. Xu, N. Zhao, *Adv. Funct. Mater.* **2015**, *25*, 1120.

[13] a) J. A. Aguiar, S. Wozny, T. G. Holesinger, T. Aoki, M. K. Patel, M. Yang, J. J. Berry, M. Al-Jassim, W. Zhou, K. Zhu, *Energy Environ. Sci.* **2016**, *9*, 2372; b) Q. Han, S.-H. Bae, P. Sun, Y.-T. Hsieh, Y. Yang, Y. S. Rim, H. Zhao, Q. Chen, W. Shi, G. Li, *Adv. Mater.* **2016**, *28*, 2253.

[14] P. Docampo, T. Bein, *Acc. Chem. Res.* **2016**, *49*, 339.

[15] a) M. Saliba, T. Matsui, J.-Y. Seo, K. Domanski, J.-P. Correa-Baena, M. K. Nazeeruddin, S. M. Zakeeruddin, W. Tress, A. Abate, A. Hagfeldt, M. Gratzel, *Energy Environ. Sci.* **2016**, *9*, 1989; b) Z. Li, M. Yang, J.-S. Park, S.-H. Wei, J. J. Berry, K. Zhu, *Chem. Mater.*

© 2016 WILEY-VCH Verlag GmbH & Co. KGaA, Weinheim

2016, *28*, 284; c) J.-W. Lee, D.-H. Kim, H.-S. Kim, S.-W. Seo, S. M. Cho, N.-G. Park, *Adv. Energy Mater.* **2015**, *5*, 201501310; d) C. Yi, J. Luo, S. Meloni, A. Boziki, N. Ashari-Astani, C. Gratzel, S. M. Zakeeruddin, U. Rothlisberger, M. Gratzel, *Energy Environ. Sci.* **2016**, *9*, 656.

[16] a) W. S. Yang, J. H. Noh, N. J. Jeon, Y. C. Kim, S. Ryu, J. Seo, S. I. Seok, *Science* **2015**, *348*, 1234; b) D. Bi, W. Tress, M. I. Dar, P. Gao, J. Luo, C. Renevier, K. Schenk, A. Abate, F. Giordano, J.-P. Correa Baena, J.-D. Decoppet, S. M. Zakeeruddin, M. K. Nazeeruddin, M. Grätzel, A. Hagfeldt, *Sci. Adv.* **2016**, *2*, e1501170.

[17] A. Binek, F. C. Hanusch, P. Docampo, T. Bein, *J. Phys. Chem. Lett.* **2015**, *6*, 1249.

[18] T. Leijtens, G. E. Eperon, N. K. Noel, S. N. Habisreutinger, A. Petrozza, H. J. Snaith, *Adv. Energy Mater.* **2015**, *5*, 201500963.

[19] a) D. B. Mitzi, in *Progress in Inorganic Chemistry*, Vol. *48*, (Ed: K. D. Karlin), John Wiley & Sons Inc, New York **1999**, p. 1; b) D. B. Mitzi, C. A. Feild, W. T. A. Harrison, A. M. Guloy, *Nature* **1994**, *369*, 467.

[20] a) B. Saparov, D. B. Mitzi, *Chem. Rev.* **2016**, *116*, 4558; b) D. B. Mitzi, *J. Chem. Soc.-Dalton Trans.* **2001**, *1*, 1.

[21] a) L. N. Quan, M. Yuan, R. Comin, O. Voznyy, E. M. Beauregard, S. Hoogland, A. Buin, A. R. Kirmani, K. Zhao, A. Amassian, D. H. Kim, E. H. Sargent, *J. Am. Chem. Soc.* **2016**, *138*, 2649; b) D. H. Cao, C. C. Stoumpos, O. K. Farha, J. T. Hupp, M. G. Kanatzidis, *J. Am. Chem. Soc.* **2015**, *137*, 7843.

[22] a) K. Liang, D. B. Mitzi, M. T. Prikas, *Chem. Mater.* **1998**, *10*, 403; b) T. M. Koh, V. Shanmugam, J. Schlipf, L. Oesinghaus, P. Müller-Buschbaum, N. Ramakrishnan, V. Swamy, N. Mathews, P. P. Boix, S. G. Mhaisalkar, *Adv. Mater.* **2016**, *28*, 3653.

[23] J. S. Manser, P. V. Kamat, *Nat. Photonics* **2014**, *8*, 737.

[24] Y. Hu, J. Schlipf, M. Wussler, M. L. Petrus, W. Jaegermann, T. Bein, P. Müller-Buschbaum, P. Docampo, *ACS Nano* **2016**, *10*, 5999.

[25] a) C.-Z. Li, C.-C. Chueh, H.-L. Yip, K. M. O'Malley, W.-C. Chen, A. K.-Y. Jen, *J. Mater. Chem.* **2012**, *22*, 8574; b) J. H. Kim, P.-W. Liang, S. T. Williams, N. Cho, C.-C. Chueh, M. S. Glaz, D. S. Ginger, A. K.-Y. Jen, *Adv. Mater.* **2015**, *27*, 695.

[26] a) J. Bisquert, I. Mora-Sero, F. Fabregat-Santiago, *ChemElectroChem* **2014**, *1*, 289; b) J. Bisquert, *J. Phys. Chem. B* **2002**, *106*, 325; c) V. Gonzalez-Pedro, E. J. Juarez-Perez, W.-S. Arsyad, E. M. Barea, F. Fabregat-Santiago, I. Mora-Sero, J. Bisquert, *Nano Lett.* **2014**, *14*, 888.

[27] a) M. Bag, L. A. Renna, R. Y. Adhikari, S. Karak, F. Liu, P. M. Lahti, T. P. Russell, M. T. Tuominen, D. Venkataraman, *J. Am. Chem. Soc.* **2015**, *137*, 13130; b) A. Guerrero, G. Garcia-Belmonte, I. Mora-Sero, J. Bisquert, Y. S. Kang, T. J. Jacobsson, J.-P. Correa-Baena, A. Hagfeldt, *J. Phys. Chem. C* **2016**, *120*, 8023; c) H.-S. Kim, I. Mora-Sero, V. Gonzalez-Pedro, F. Fabregat-Santiago, E. J. Juarez-Perez, N.-G. Park, J. Bisquert, *Nat. Commun.* **2013**, *4*, 2242.

[28] Y. Shao, Z. Xiao, C. Bi, Y. Yuan, J. Huang, *Nat. Commun.* **2014**, *5*, 5784.

[29] a) F. Fabregat-Santiago, G. Garcia-Belmonte, I. Mora-Sero, J. Bisquert, *Phys. Chem. Chem. Phys.* **2011**, *13*, 9083; b) A. Dualeh, T. Moehl, N. Tétreault, J. Teuscher, P. Gao, M. K. Nazeeruddin, M. Grätzel, *ACS Nano* **2014**, *8*, 362.

© 2016 WILEY-VCH Verlag GmbH & Co. KGaA, Weinheim